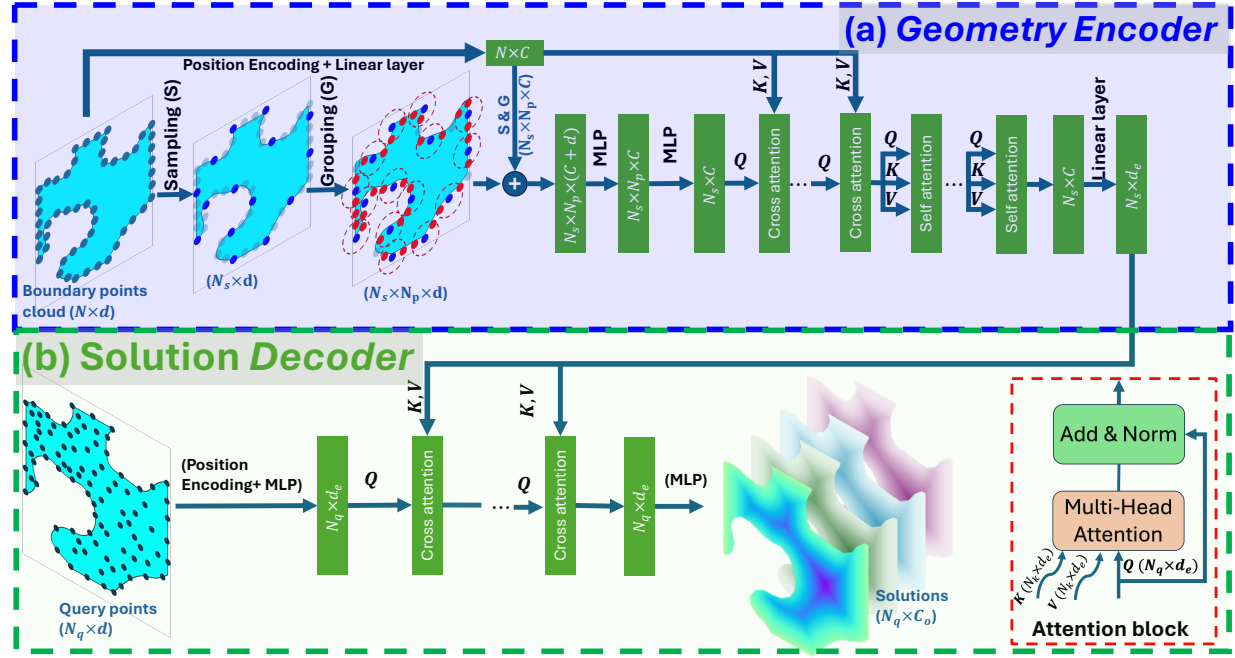


Graphical Abstract

Geometry-Informed Neural Operator Transformer

Qibang Liu, Weiheng Zhong, Hadi Meidani, Diab Abueidda, Seid Koric, Philippe Geubelle



Highlights

Geometry-Informed Neural Operator Transformer

Qibang Liu, Weiheng Zhong, Hadi Meidani, Diab Abueidda, Seid Koric, Philippe Geubelle

- A Geometry-Informed Neural Operator Transformer (GINOT) is proposed for forward predictions on arbitrary geometries
- GINOT encodes surface point clouds that are unordered, have non-uniform point density, and varying numbers of points.
- GINOT effectively processes complex, arbitrary geometries and varying input conditions with good predictive accuracy

Geometry-Informed Neural Operator Transformer

Qibang Liu^{a,g,*}, Weiheng Zhong^e, Hadi Meidani^e, Diab Abueidda^{a,f}, Seid Koric^{a,d} and Philippe Geubelle^{b,c}

^a*National Center for Supercomputing Applications, University of Illinois Urbana-Champaign, Urbana, 61801, IL, USA*

^b*Beckman Institute for Advanced Science and Technology, University of Illinois Urbana-Champaign, Urbana, 61801, IL, USA*

^c*The Grainger College of Engineering, Department of Aerospace Engineering, University of Illinois Urbana-Champaign, Urbana, 61801, IL, USA*

^d*The Grainger College of Engineering, Department of Mechanical Science and Engineering, University of Illinois Urbana-Champaign, Urbana, 61801, IL, USA*

^e*The Grainger College of Engineering, Department of Civil and Environmental Engineering, University of Illinois Urbana-Champaign, Urbana, 61801, IL, USA*

^f*Civil and Urban Engineering Department, New York University Abu Dhabi, United Arab Emirates*

^g*Department of Industrial and Manufacturing Systems Engineering, Kansas State University, Manhattan, 66506, KS, USA*

ARTICLE INFO

Keywords:

Transformer

Geometry-informed

Neural operator

Arbitrary geometry

Point cloud

Deep learning

ABSTRACT

Machine-learning-based surrogate models offer significant computational efficiency and faster simulations compared to traditional numerical methods, especially for problems requiring repeated evaluations of partial differential equations. This work introduces the Geometry-Informed Neural Operator Transformer (GINOT), which integrates the transformer architecture with the neural operator framework to enable forward predictions on arbitrary geometries. GINOT employs a sampling and grouping strategy together with an attention mechanism to encode surface point clouds that are unordered, exhibit non-uniform point densities, and contain varying numbers of points for different geometries. The geometry information is seamlessly integrated with query points in the solution decoder through the attention mechanism. The performance of GINOT is validated on multiple challenging datasets, showcasing its accuracy and generalization capabilities for complex and arbitrary 2D and 3D geometries.

1. Introduction

Many natural phenomena in the physical world are governed by partial differential equations (PDEs), which encapsulate fundamental principles of physics. Numerical techniques such as finite difference, finite element, and finite volume methods have been developed to solve these equations computationally. While these methods enable high-resolution simulations to capture complex physical behaviors, they often demand significant computational resources, making them time-intensive, costly, and sometimes infeasible under current computational limitations.

Data-driven surrogate models have emerged to alleviate these computational burdens. Leveraging deep neural architectures, they approximate PDE solution operators with substantial speedups while retaining acceptable accuracy, making them effective when many evaluations are required [1]. Typical downstream tasks include sensitivity analysis [2, 3], gradient-based optimization [4, 5], uncertainty quantification [6–8], digital twins [9–11], and inverse or generative design [12, 13]. These surrogates do not replace a single high-fidelity simulation; rather, they amortize its upfront cost over large query workloads, enabling dramatically faster iterative engineering and design cycles.

Neural operators have become prominent surrogate models, adept at mapping infinite-dimensional input functions to output functions at specified query points:

$$G_\theta : \mathcal{F} \rightarrow \mathcal{G}(\mathbf{x}), \quad (1)$$

where G_θ is the neural operator with learnable parameter θ , \mathcal{F} is the space of input functions, and \mathcal{G} is the space of output functions on query points \mathbf{x} . Examples such as the Fourier Neural Operator (FNO) [14] and the Deep Operator Network (DeepONet) [15] have shown significant success in this area [16–25]. These models map inputs like initial

*Corresponding author

Email address: qibang@illinois.edu (Q. Liu)

and boundary conditions, material properties, and other functions to solution fields at query points. However, their applicability is often limited to simple geometries. For instance, FNO is tailored for fixed, regular meshes such as image grids or 3D voxels and requires a complete mesh graph as input due to its reliance on the Fast Fourier Transform kernel, making it unsuitable for arbitrary geometries and less scalable. While DeepONet can predict solution fields at arbitrary query points, its original formulation is restricted to single geometries with fixed query point locations and counts.

However, real-world problems frequently involve complex and arbitrary computational geometries. Recent advances, including graph neural operators (GNO) [26], Geo-FNO [27], GI-FNO [28], and Geom-DeepONet [29], have addressed challenges in handling diverse geometries. GNO can process irregular grids using graph representations but is limited to local operations under constrained computational budgets, resulting in lower accuracy. Both Geo-FNO and GI-FNO rely on projecting irregular meshes onto fixed regular grids and mapping them back. However, Geo-FNO requires a fixed number of query points during training, while GI-FNO constructs new graphs on regular meshes using local kernel integration layers through GNO, which need longer inference time. Geom-DeepONet, while overcoming the limitation of single geometries of DeepONet by removing or repeating nodes to ensure fixed data size, is restricted to parametric geometries (e.g., length, thickness, radius) and does not generalize to fully arbitrary shapes. Additionally, GI-FNO requires a signed distance function (SDF) as input to represent geometry, and Geom-DeepONet depends on both geometry parameters and the SDF. However, obtaining the SDF is not always easily, particularly for complex 3D geometries represented by surface meshes, as it incurs a computational cost of $O(N_g \times N_m)$ for distance calculation and $O(N_g \times N_m)$ for the minimum value, where N_g is the number of grid points in the domain and N_m is the number of surface mesh—both of which are large for intricate geometries.

Researchers have leveraged the attention mechanism of transformers [30] in neural operators to efficiently integrate information from input functions and query points [31–34]. Neural Operator Transformers (NOT) are particularly advantageous for irregular meshes due to their attention mechanism, enabling the prediction of solution fields at arbitrary query points. Unlike DeepONet, which employs a simple dot product to combine information from input functions and query points, the attention mechanism in NOT directs each query point to focus on the most relevant information from the input functions. This capability allows NOT to generalize effectively and capture more complex relationships between input functions and query points. Building on this, the authors developed an SDF-based NOT that accommodates arbitrary geometries [13]. The SDF representation facilitates handling arbitrary geometries on fixed, regular grids, which are compatible with existing deep learning models. However, as noted earlier, obtaining the SDF is not always straightforward or computationally easily.

In this work, we introduce the Geometry-Informed Neural Operator Transformer (GINOT), which integrates the transformer architecture with the neural operator framework to enable forward predictions for arbitrary geometries without requiring SDF as geometry features. GINOT consists of two primary components: the geometry encoder and the solution decoder. Drawing inspiration from Shap-E [35] by OpenAI, we design the geometry encoder to process the boundary point cloud, representing the geometry, into the KEY and VALUE matrices for the attention mechanism. This choice facilitates the integration of information from query points in the solution decoder.

The geometry encoder utilizes sampling and grouping layers [36, 37] to extract local geometric features from the boundary point cloud. These local features are fused with global geometry information through cross-attention layers, enabling effective processing of unordered and non-uniformly distributed point clouds—unlike convolutional neural networks (CNNs), which operate on regular grids with uniform density. Because the number of points in the point cloud can vary between geometries, padding is applied to standardize input sizes within a batch. To ensure that padding points do not influence the geometry encoder’s output, a masking mechanism is employed: it prevents padding points from being selected in the sampling and grouping layers and excludes them from contributing to attention scores in the cross-attention layer.

In addition to varying geometries, many problems involve additional input parameters such as loading, material properties, and boundary conditions. To address such cases, we propose an extension strategy for GINOT by incorporating additional encoders to process these input functions.

This manuscript summarizes the key concepts, methodologies, and results of the GINOT model. We validate the effectiveness of GINOT on multiple challenging datasets and compare its performance with baseline methods. The results demonstrate that GINOT achieves high accuracy and generalizes effectively to arbitrary geometries.

2. GINOT

GINOT integrates the transformer architecture with the neural operator framework to enable forward predictions for arbitrary geometries. It consists of two primary components: the geometry encoder and the solution decoder, as illustrated in Fig. 1. Both components leverage the attention mechanism inherent in the transformer architecture [30], which facilitates the model’s ability to focus on relevant input information. The attention mechanism is defined as

$$\text{Attention}(Q, K, V) = \text{softmax} \left(\frac{QK^T}{\sqrt{d_e}} \right) V, \quad (2)$$

where $Q \in \mathbb{R}^{N_q \times d_e}$ represents the QUERY matrix, and $K, V \in \mathbb{R}^{N_k \times d_e}$ are the KEY and VALUE matrices, respectively. Here, d_e denotes the embedding dimension, N_q is the length of the query sequence, and N_k is the length of the KEY and VALUE sequences. To ensure stable training, residual connections and layer normalization are applied within each attention block, as depicted in the bottom right of Fig. 1.

In the following sections, we detail the GINOT architecture, omitting the batch size dimension for simplicity. For instance, we describe the points cloud as having dimensions $N \times d$, where N represents the number of points and d denotes the dimensionality. In practice, the actual shape of the points cloud is $B \times N \times d$, with B being the batch size.

2.1. Geometry encoder

Traditional convolutional architectures rely on highly regular input formats, such as image grids or 3D voxels, to efficiently perform kernel operations. While effective for structured data, these formats are unsuitable for capturing arbitrary geometries. In contrast, boundary points clouds offer a flexible representation for arbitrary geometries but lack the regularity required by convolutional architectures, presenting unique challenges for processing.

To address these challenges, we developed a geometry encoder that processes the boundary point cloud of a geometry into the KEY and VALUE matrices for the attention mechanism. This enables seamless integration of geometry information with query points in the solution decoder. In contrast to CNN inputs, boundary point cloud used to represent geometries have three key characteristics: (1) invariance to the order of points, (2) non-uniform point density across locations, and (3) a variable number of points across geometries. Drawing inspiration from Shap-E [35] by OpenAI, the geometry encoder, as shown in Fig. 1(a), is designed to handle these characteristics. It ensures invariance to point order and padding while maintaining robustness to variations in point density.

The point cloud is first processed through a sampling layer and a grouping layer for local geometry features, originally introduced in PointNet [36] and PointNet++ [37], which are well-suited to handle the aforementioned properties. The sampling layer employs the iterative farthest point sampling (FPS) method [37] to select N_s points from the point cloud. This method begins by randomly selecting a point, then iteratively selects the farthest point from the already selected points until N_s points are chosen. Compared to random sampling, the FPS method provides better coverage of the entire point set for a given number of centroids. The selected points are then passed to the grouping layer, which forms N_s groups, each containing N_p points.

For each group, the N_p points are selected as those within a ball of radius r (a hyperparameter) centered at the corresponding sampled point. If fewer than N_p points exist within the ball, the group is padded with the nearest points to the center. Conversely, if more than N_p points are present, the nearest N_p points are chosen. Consequently, the output of the grouping layer has dimensions $N_s \times N_p \times d$, where d represents the dimensionality of the point cloud. The sampling and grouping layers allow to extract local geometry features from nonuniform density point cloud [37]. These layers output the selected points along with their indices in the original point cloud, which are subsequently used in downstream layers.

The point cloud is also processed through a positional encoder layer utilizing the Nerf encoding method [38], followed by a linear layer. Using the indices from the sampling and grouping layers, the output is indexed to extract local geometry information, resulting in a tensor of shape $N_s \times N_p \times C$, where C represents the output channel dimension of the positional encoder. This tensor is concatenated with the output of the grouping layer. The combined tensor is then passed through a series multi-layer perceptron (MLP) layers, which aggregates the information within each group, reducing the dimension of N_p to 1. As a result, the final output has a shape of $N_s \times C$.

The local information obtained by the sampling and grouping layers is utilized as the QUERY (Q) in the cross-attention blocks, while the KEY (K) and VALUE (V) are derived from the output of the positional encoder layer, which captures global geometry information. The attention mechanism allows the local information in the QUERY

(Q) to focus on the relevant global geometry features. The QUERY (Q) can be invariant to the permutation of points order based on the sampling and grouping mechanism, whereas the KEY (K) and VALUE (V) depend on the order of points as they are directly derived from the positional encoder layer with the point cloud as input. However, the output of the cross-attention block remains invariant to the order of points because of:

$$\text{Attention}(Q, K, V)_{id} = \text{softmax} \left(\frac{Q_{ij} K_{mj}}{\sqrt{d_e}} \right) V_{md}, \quad (3)$$

where the output is unaffected by permutations of the index m , which is a dummy index under Einstein summation notation. To ensure strict invariance, the sampling and grouping layers must also be invariant to the permutation of the point cloud. This requires consistently selecting the same initial point in the iterative FPS sampling layer and grouping points based on their distance to the centroids chosen by the sampling layer. However, as the sampling and grouping layers can sufficiently extract the geometry features regardless of the initial point selection, we use random initialization of the first point during FPS iteration in training. During inference, the first point is fixed as the first non-padding point of the point cloud to ensure consistent results. Our experiments demonstrate that this random initialization has a negligible impact on GINOT's output (as shown in Section 3.5).

The computational cost of the sampling and grouping layers is mainly attributed to the FPS and ball query operations. The FPS step, which iteratively selects the farthest point by computing distances between all pairs of points in the point cloud, has a complexity of $O(N^2)$. The ball query step, which identifies points within a specified radius around each sampled point, involves a complexity of $O(N \times N_s)$, where N is the total number of points in the point cloud and N_s is the number of sampled points. Importantly, both N and N_s are typically much smaller than the number of grid points and surface mesh points required in SDF-based methods, making the sampling and grouping layers in GINOT computationally more efficient, as further elaborated in Section 3.6.

The sampling and grouping layers, combined with the attention mechanism, allow that the geometry encoder handle the point cloud with varying points density, while remaining robust to the permutation of points order. Since the number of points in the point cloud varies across different geometries, padding is typically required to standardize input sizes within a batch for deep learning models. To prevent padding points from influencing the geometry encoder's output, a masking mechanism is employed. This mechanism excludes padding points from being selected in the sampling and grouping layers. Additionally, padding points can interfere with attention scores in the cross-attention layer of the geometry encoder. To mitigate this, the corresponding entries in the attention score matrix $(Q \cdot K^T) / \sqrt{d_e}$ are set to " $-\infty$ ", ensuring that the attention layer's output is unaffected by padding points. The flexibility and robustness of the proposed geometry encoder are illustrated in experiments Section 3.

2.2. Solution decoder

The solution decoder predicts the solution field at the query points using the geometry information from the geometry encoder. First, the query points are processed through a Nerf positional encoding, followed by an MLP, to generate the QUERY matrix with dimensions $N_q \times d_e$, where N_q is the number of query points and d_e is the embedding dimension. This QUERY matrix is then passed into cross-attention layers, which integrate the geometry information from the geometry encoder. The attention mechanism ensures that the query points focus on the most relevant geometry features. Finally, the output of the cross-attention layers is decoded into the solution field at the query points using another MLP. The architecture of the solution decoder is illustrated in Fig. 1(b).

Since the geometries are arbitrary, the number of query points varies across different geometries. To handle this variability, GINOT processes batches of geometries by padding the query points to match the maximum count within each batch, similar to techniques used for variable sequence lengths in natural language processing.

2.3. Extending GINOT

Many problems involve not only varying geometries but also additional input parameters, such as loading conditions, material properties, or boundary conditions. To address such cases, GINOT can be extended by incorporating additional encoders to process these input functions. The outputs of these additional encoders are concatenated with the output of the geometry encoder and passed through an MLP for aggregation of all information from the geometries and the additional inputs. The aggregated output is then used as the KEY and VALUE in the cross-attention blocks of the solution decoder. The architecture of the extended GINOT is illustrated in Fig. 2. This extension is demonstrated in the bracket lug example in Section 3.4, where varying loading conditions are included as additional inputs.

Table 1

Dataset overview.

DataSet	Elasticity[27]	Poisson (structure mesh)	Poisson (unstructure mesh)	Bracket lug [29]	Micro-PUC [39]	JEB [40]
Data size	2000	6000	6000	3000	73879	2138
Number of query point	972	2737	[1566,2838]	[5054,15210]	[1136,6363]	[18085,55009]
Number points in boundary PC	105	144	144	[2184,4284]	[180,484]	[2253,10388]
Parametric	True	True	True	True	False	False
Solution	Stress	–	–	Mises stress	Mises stress displacements	Mises stress

3. Experiments

In this section, we present several numerical experiments to evaluate the performance and accuracy of GINOT on various challenging datasets. The primary evaluation metric used is the L_2 relative error defined as

$$L_2 = \frac{\|y^{\text{true}} - y^{\text{pred}}\|_2}{\|y^{\text{true}}\|_2}, \quad (4)$$

where y^{true} and y^{pred} represent the ground truth and predicted solutions, respectively.

To train the GINOT models, we use the mean square error (MSE) as the loss function. Since the number of query points is padded to match the maximum number of nodes in the batch, a masking mechanism is applied to exclude the padding points from the loss calculation:

$$\text{MSE} = \frac{1}{1 + \sum_{i=1}^N m_i} \sum_{i=1}^N m_i (y_i - \hat{y}_i)^2, \quad (5)$$

where m_i is the mask value, set to 1 for non-padding points and 0 for padding points. The addition of 1 in the denominator ensures the denominator is never zero. Prior to training, both input and output data are normalized to have zero mean and unit variance.

This section provides an overview of the datasets used in the experiments, along with the training hyperparameters and computational efficiency of GINOT for these datasets. Additionally, we summarize GINOT's performance on these datasets and compare it with baseline methods. Detailed experimental results are presented in the subsequent subsections. Further implementation details and results can be found in our GitHub repository.

3.1. Overview

To evaluate the performance and accuracy of GINOT, six datasets are utilized: elasticity [27], Poisson equation with both structured and unstructured meshes, bracket lugs [29], micro-periodic unit cell (PUC) [39] in [13], and Jet Engine Bracket (JEB) [40]. Table 1 provides a detailed summary of these datasets, including their size, the number of query points, the number of points in the boundary point cloud, whether the dataset is parametric or fully arbitrary, and the type of solution considered. The first three datasets have a constant number of points in the boundary point cloud, while the last three datasets feature a varying number of points in the boundary point cloud. All datasets feature non-uniform point densities, as illustrated in the visualization results in the following subsections. While the datasets considered here focus on representative linear and nonlinear single-physics cases, the framework is not confined to single-physics or weakly coupled settings. With suitably generated training data, it works for complex, strongly coupled multi-physics problems.

Table 2 summarizes the training hyperparameters of the GINOT models. For the micro PUC dataset, two models are trained: one for predicting the solution at the final strain step and another for predicting the solution over historical strain steps.

Table 3 summarizes the computational efficiency of GINOT. Training tasks were conducted on single NVIDIA A100 GPU on the DELTA machine or single NVIDIA H100 GPU on the DeltaAI machine, both hosted at the National

Table 2

Training hyperparameters of the GINOT models. All models are implemented with the PyTorch scheduler *ReduceLROnPlateau*.

	Elasticity	Poisson (structure mesh)	Poisson (unstructure mesh)	Bracket lug	Micro PUC (Final strain step)	Micro PUC (historical strain steps)	JEB
Batch size	20	32	32	32	64	64	16
Optimizer	Adam	Adam	Adam	Adam	Adam	Adam	AdamW
Initial learning rate	0.001	0.001	0.001	0.001	0.001	0.001	0.0005
scheduler Patience	40	40	40	20	10	10	100
scheduler Factor	0.7	0.7	0.7	0.7	0.7	0.7	0.7
Epochs	1000	500	500	500	400	500	500
Training dataset	1000	80%	80%	80%	80%	80%	90%
Testing dataset	200	20%	20%	20%	20%	20%	10%
N_s	16	64	64	512	128	128	512
N_p	18	18	18	64	8	8	64
Grouping r	0.2	0.2	0.2	0.5	0.1	0.2	0.1
Att. heads (Decoder)	4	8	8	8	4	4	4
Attention heads (Encoder)	4	8	8	8	8	8	1
Cross att. layers (Encoder)	1	1	1	1	2	2	1
Self att. layers (Encoder)	2	3	3	2	2	2	2
Cross att. layers (Decoder)	6	4	4	3	4	4	4

Table 3

GINOT computation efficiency.

	Elasticity	Poisson (structure mesh)	Poisson (unstructure mesh)	Bracket lug	Micro PUC (Final strain step)	Micro PUC (historical strain steps)	JEB
Training GPU	A100	A100	A100	H100	H100	H100	H100
Training [s/epoch]	1.7	12.1	11.9	33.2	128	136	31
Inference [s/solution]	3.94e-4	1.03e-3	9.2e-4	1.35e-2	2.18e-3	4.82e-3	4.0e-2

Center for Supercomputing Applications (NCSA) at the University of Illinois Urbana-Champaign (UIUC). Inference tasks were executed on single NVIDIA A100 GPU on the DELTA machine.

Table 4 summarizes GINOT’s performance across the datasets, presenting the L_2 relative error for both training and testing samples. These results are compared against baseline methods, with the best performance highlighted in bold. The findings demonstrate GINOT’s ability to tackle more complex problems while outperforming the baseline methods. Detailed experimental results are provided in the subsequent subsections.

3.2. Elasticity

For the elasticity example, we utilized the dataset generated by Li et al. [27] for training the Geo-FNO model. The dataset consists of unit cells of $[0, 1]^2$ with arbitrary-shaped voids at the center, as illustrated in Fig. 3. The central void is defined by 45 points evenly distributed along the tangential direction, parameterized as

$$\begin{aligned} x_i &= r_i \cos(\theta_i), \\ y_i &= r_i \sin(\theta_i), \end{aligned} \quad (6)$$

where r_i is the radius of the i -th point, and $\theta_i = (2\pi i)/45$. The radii r_i follow a Gaussian distribution, constrained within $0.2 \leq r_i \leq 0.4$. The unit cell is fixed at the bottom and a tensile traction is applied at the top to simulate the stress field. The dataset uses a structured mesh with a fixed number of 972 nodes across all samples. A total of 1000 training samples were used to train the model for predicting stress solutions for various geometries.

Geo-FNO [27] employs 45 parametric void radii as geometry features, which limits its applicability to parametric geometries. In contrast, GINOT uses boundary points clouds to represent geometry, enabling it to handle arbitrary geometries. The stress solutions of the testing samples predicted by GINOT are shown in Fig. 3, highlighting the

Table 4

Performance comparison of GINOT with baseline methods. “–” indicates that the method cannot handle the dataset, while “NA” signifies that the method can handle the dataset but results are unavailable. The best performance is highlighted in bold.

Dataset, Metric	Data	Geo-FNO[27]	Geom-DeepONet[29]	GNO[26]	GI-FNO[28]	GINOT
Elasticity, L_2	Training	1.25%	NA	11.3%	1.32%	0.806%
	Testing	2.29%	NA	12.3%	1.66%	1.03%
Poisson, L_2 (structure mesh)	Training	0.43%	NA	7.43%	0.42%	0.39%
	Testing	0.48%	NA	7.82%	0.45%	0.437%
Poisson, L_2 (unstructure mesh)	Training	–	NA	7.98%	0.49%	0.41%
	Testing	–	NA	8.23%	0.55%	0.53%
Bracket lug, L_2	Training	–	1.818%	10.5%	2.51%	0.35%
	Testing	–	1.824%	11.3%	2.81%	0.40%
Micro PUC, L_2 (Final strain step)	Training	–	–	16.5%	9.24%	6.99%
	Testing	–	–	18.2%	9.95%	7.61%
Micro PUC, L_2 (historical strain steps)	Training	–	–	18.9%	9.56%	8.42%
	Testing	–	–	19.5%	10.01%	9.06%
JEB, L_2	Training	–	–	36.4%	27.5%	18.77%
	Testing	–	–	67.3%	31.4%	30.77%

median and worst cases in terms of L_2 relative error. For the median case, the L_2 relative error is 0.96%, while the worst case has an L_2 relative error of 2.31%. The mean L_2 relative error across the testing samples is 1.03%, with a standard deviation of 0.35%.

3.3. Poisson equation

The Poisson equation considered in this study is given by

$$\begin{aligned} -\nabla^2 u &= f, \quad \text{in } \Omega, \\ u &= g, \quad \text{on } \partial\Omega, \end{aligned} \tag{7}$$

where Ω represents the domain, u is the solution, f is the source term, and g is the Dirichlet boundary condition. For all samples, we set $f = 1$ and $g = 0$. Similar to the elasticity example, the domain Ω is parameterized using Eq. (6), with the radius $r_i \in [0.2, 0.8]$ and $i = 1, 2, \dots, 144$. The geometries are illustrated in Fig. 4.

Two datasets were generated for this problem, each containing 6000 samples. The first dataset uses a structured mesh with a fixed 2737 nodes across all samples, while the second dataset employs an unstructured mesh, where the number of nodes varies between 1566 and 2838. The structured and unstructured meshes are illustrated in the last column of Fig. 4. For comparison with Geo-FNO, which does not support unstructured meshes with varying node counts, we focus on the structured mesh dataset. The Poisson equation was solved using FEM with FEniCSX. Of the total samples, 20% were reserved for testing, and the remaining 80% were used for training.

The comparison between GINOT predictions and the ground truth is presented in Fig. 4. For the unstructured mesh dataset, the median case has an L_2 relative error of 0.41%, while the worst case has an L_2 relative error of 2.27%. For the structured mesh dataset, only the median case is shown for brevity, with an L_2 relative error of 0.38%. The mean L_2 relative error for the testing samples of the structured mesh dataset is 0.45%, with a standard deviation of 0.17%, while for the unstructured mesh dataset, the mean L_2 relative error is 0.44%, with a standard deviation of 0.21%.

3.4. Bracket lug

We address the plasticity problem of bracket lugs using the dataset used in [29]. The bracket lugs, depicted in Fig. 5, are parameterized by three variables: length, thickness, and the radius of the circular hole. FEM simulations employ an elastic-plastic material model with linear isotropic hardening and quadratic hexahedral elements under small deformation assumptions. For training GINOT, the middle edge nodes of the quadratic hexahedral elements are removed. The surface mesh is extracted from the volume hexahedral elements, and its nodes are used as the boundary point cloud, which is then input to the geometry encoder of GINOT.

The dataset also includes variations in pressure loading across samples. To incorporate the loading parameter, we adopt the framework shown in Fig. 2. An MLP encodes the loading (shape of $B \times 1$) into a tensor with shape of $B \times d_e$, which is expanded to $B \times N_s \times d_e$ by repeating the tensor N_p times, where B is the batch size. This tensor is concatenated with the geometry encoder's output and passed through an MLP, whose output serves as the KEY and VALUE for the attention mechanism. The dataset contains 3000 samples, with 20% reserved for testing.

The stress solutions for the testing samples predicted by GINOT are shown in Fig. 5, highlighting the median and worst cases based on L_2 relative error. The median case has an L_2 relative error of 0.41%, while the worst case reaches 3.78%. The mean L_2 relative error for the testing samples is 0.45%, with a standard deviation of 0.23%.

3.5. Micro-periodic unit cell

The previous examples focus on 2D or 3D geometries with relatively simple shapes parameterized by a few variables. In this example, we consider micro-periodic unit cells (PUC) generated by the authors for metamaterial architecture design. These geometries are more complex and fully arbitrary. The dataset is created by first generating a 2D periodic Gaussian random field on a square domain $[0, 1 \text{ mm}]^2$. The Marching Squares algorithm is then applied to extract the contour at a random threshold value, defining the boundary of the 2D periodic unit cell, with field values below the threshold treated as void.

Periodic boundary conditions and compression are applied to the unit cell for FEM simulations to obtain the mechanical response field. The simulations use an elasto-plastic material model with large deformation within the environment of Abaqus. To approximate quasi-static compression while improving convergence for large deformation and elasto-plastic behavior, an implicit dynamic solver is employed with a virtual mass density of $\rho = 10^{-8}$. The compression strain is applied smoothly over 51 steps from $\epsilon = 0$ to $\epsilon = 20\%$. The simulation utilizes a combination of mixed first-order quadrilateral elements and second-order triangular elements with full integration. To augment the dataset, the unit cell is randomly shifted multiple times. The corresponding stress and displacement solution fields are also shifted accordingly, enabling data augmentation without additional FEM simulations. The boundary point cloud of the geometry is formed by combining the points on the contours from the Marching Squares algorithm and the points on the boundary of the square domain, spaced at intervals of $\frac{1}{32} \text{ mm}$. This boundary point cloud represents the geometry features and is fed into the geometry encoder.

The dataset comprises around 73,879 samples, with 20% reserved for testing. The GINOT model is trained to predict Mises stress and two displacement components, both at the final strain step and over historical strain steps.

The predicted solutions at the final strain step are shown in Fig. 6, comparing the ground truth with GINOT predictions. The first row highlights the median case with an L_2 relative error of 7.54%, while the second row shows the 95th percentile case with an L_2 relative error of 13.03%. The first column illustrates the input surface point cloud, the second column presents the true stress on the true deformed shape, the third column displays the predicted stress on the predicted deformed shape, and the last column shows the absolute error of stress on the true deformed shape. The mean L_2 relative error across the testing samples is 9.05%, with a standard deviation of 3.53%.

The stress and displacement solutions over historical strain steps are compared with the ground truth and illustrated in Fig. 7. For brevity, only the median case is presented here. Additional cases, such as the best and worst, can be found in our [Github repository](#). The first row shows the true stress on the true deformed shape, the second row depicts the predicted stress on the predicted deformed shape, and the last row highlights the absolute error of stress on the true deformed shape. The overall L_2 relative error for historical steps is 9.08%. The mean L_2 relative error for the testing samples is 9.06%, with a standard deviation of 3.02%.

As detailed in Section 2.1, the geometry encoder in GINOT is designed to handle 1) nonuniform point cloud densities, 2) permutations in point order, and 3) padding within the point cloud. The first property is evident throughout the examples in this work. To demonstrate the latter two properties, we analyze the second-best test case in this example. Notably, GINOT maintains stable inference performance even when the point cloud is made sparser. In this analysis, the point cloud is shuffled, reduced to 80% of its original size, padded with 199 points at $(-1000, -1000)$, and shuffled again. These modified point clouds are input to the trained GINOT, with results shown in Fig. 8. The L_2 relative errors for the original, reduced and shuffled, padded, and shuffled padded point clouds are 3.75%, 3.83%, 3.75%, and 3.75%, respectively. The similar L_2 errors across these cases demonstrate the geometry encoder's robustness to point order and padding. We emphasize that the results in Fig. 8 were produced using sampling and grouping layers implemented to be invariant to point permutations as described in Section 2.1; consequently, the padded and shuffled-padded variants yield identical L_2 errors (3.75%). If a simpler FPS implementation is used that initializes from the first non-padding point (default of GINOT), the shuffled-padded case shows an increase in L_2 of only 0.002 relative to the padded case,

Table 5

Impact of point cloud density on the inference performance of the trained model.

Point cloud density (percentage of original)	100%	80%	60%	40%	20%
L_2 relative error	3.75%	3.83%	4.50%	8.18%	30.46%

indicating negligible impact. Although shuffling and padding have minimal impact on model performance, a significant reduction in point cloud density can lead to an increase in the L_2 relative error due to the loss of geometric information. The effect of point cloud density on model performance is summarized in Table 5.

3.6. Jet engine bracket

The final example demonstrating GINOT’s capability is the Jet Engine Bracket (JEB) dataset [40]. This dataset comprises 2,138 samples of jet engine brackets derived from the “GE Jet Engine Bracket Challenge” guidelines. These geometries are complex 3D structures with arbitrary shapes and sizes. FEM simulations provide solution fields (e.g., stress, displacement) under four loading scenarios: vertical, horizontal, diagonal, and torsional, all with fixed loading magnitudes. In this example, we focus on the Mises stress solution under vertical loading.

The dataset includes CAD models, volume meshes in VTK format, and solution fields on fine quadratic tetrahedral elements. Instead of extracting surface nodes from the volume mesh, we extract the boundary point cloud directly from the CAD model vertices for each JEB sample using FreeCAD with PythonAPI, as illustrated in Fig. 9(a). To reduce computational costs, the volume mesh is downgraded from 10-node tetrahedrons to 4-node tetrahedrons by removing the middle nodes of each element’s edge. The nodes of these linear tetrahedrons are then used as query points in the solution decoder of GINOT, as shown in Fig. 9(a). Fig. 9(b) illustrates the number of boundary points in the cloud and the volume mesh nodes for the 2,138 JEB samples. The boundary point cloud contains between 2,253 and 10,388 points, while the volume mesh nodes range from 18,085 to 55,009.

Fig. 10 illustrates the training process of GINOT on the JEB dataset. The mean squared error (MSE) loss for both the training and validation datasets decreases steadily during training. However, the testing loss remains significantly higher than the training loss, suggesting overfitting. This behavior is attributed to GINOT’s high representational capacity—its geometry-aware encoder and transformer decoder can closely fit intricate training patterns. The JEB dataset is comparatively small (2,138 samples) yet contains highly complex geometries. This combination of high model capacity and limited, heterogeneous data increases susceptibility to overfitting.

After training, we evaluate GINOT’s performance on both the training and testing samples. For the training samples, the mean L_2 relative error is 18.77% with a standard deviation of 4.13%, while for the testing samples, the mean L_2 relative error is 30.77% with a standard deviation of 8.86%. Fig. 11 illustrates the Mises stress solutions for the testing samples predicted by GINOT, showcasing the best, median, and worst cases in terms of L_2 relative error. The best case achieves $L_2 = 17.0\%$, while the worst case has $L_2 = 54.0\%$.

To assess efficiency relative to SDF-based neural operators, the signed distance function was computed on a 128^3 grid for first 3D test geometry (39k surface mesh triangles). The SDF evaluation required about 30 s on an A100 GPU, whereas GINOT’s sampling and grouping step took about 9 ms. This speed advantage shows that the proposed sampling and grouping strategy is substantially more efficient than explicit SDF construction for complex 3D geometries.

3.7. Ablation study

Finally, we conducted an ablation study to evaluate the impact of different configurations of our model.

The geometry encoder in our model includes cross-attention blocks followed by self-attention blocks. To assess the importance of these components, we performed experiments on the 2D PUC dataset and the 3D lug dataset. The results, summarized in Table 6, are presented in terms of L_2 relative errors.

The study reveals that the cross-attention block is crucial, as its removal significantly increases the L_2 error. This is because the cross-attention block effectively encodes global geometric features from the boundary point cloud. On the other hand, the self-attention block’s necessity varies: its removal increases the L_2 error for the PUC dataset but decreases it for the lug dataset. This discrepancy is likely attributed to the higher complexity and randomness of the 2D PUC dataset compared to the parametric 3D lug dataset, where the self-attention block aids in learning better geometric representations for the more complex dataset.

Table 6Ablation study results showing the L_2 relative errors for different attention block configurations.

	2D PUC [%]	3D LUG [%]
Full model	7.81	0.40
Without cross-attention block	12.50	0.42
Without self-attention block	10.77	0.384
Without both cross- and self-blocks	21.84	0.389

Table 7Ablation study results showing the L_2 relative errors (%) for different sampling and grouping configurations: number of sampled centroids N_s , points per group N_p , and grouping radius r . "—" indicates that the configuration was not tested.

N_s	PUC	Elasticity	N_p	PUC	Elasticity	r	PUC	Elasticity	LUG	JEB
8	—	1.09	8	7.81	1.27	0.1	7.61	1.25	0.41	30.77
16	8.99	1.03	18	8.33	1.33	0.2	7.81	1.33	0.43	30.84
32	8.27	1.16	32	7.46	1.36	0.4	8.98	1.30	—	—
64	7.97	1.33	64	7.40	1.25	0.5	9.23	1.53	0.40	31.70
96	—	1.49								
128	7.81	—								

Table 8Ablation on PC density for dataset of PUC. Reported are L_2 relative errors (%) when evaluating with the same density as training or with the full (100%) point cloud.

Training PC density (% of original)	L_2 when eval. with same density	L_2 when eval. with 100% PC
100%	7.94	7.94
80%	8.49	8.99
60%	9.65	9.44
40%	11.46	10.22

We further examine the impact of the sampling and grouping hyperparameters in Table 7. We vary the number of sampled centroids (N_s), the points per group (N_p), the grouping radius (r), and report the relative L_2 error on the PUC, Elasticity, LUG, and JEB datasets. For Elasticity (105 boundary points), changing percentage of sampling points ($N_s/105$) from 7.6% to 30% yields similar accuracy, while increasing it to 61-91% degrades performance, likely because information become overly global. For PUC (up to 484 boundary points), increasing $N_s/484$ from 3.3% to 26.4% steadily improves accuracy, with diminishing returns beyond roughly 20-26%. A practical choice is N_s at about 15-30% of the boundary points. The effect of N_p is relatively minor on both PUC and Elasticity within the tested range. The grouping radius r controls neighborhood size: smaller radii ($r = 0.1-0.2$) generally perform best, whereas larger radii ($r = 0.4-0.5$) tend to blend unrelated regions and may slightly hurt accuracy. We therefore recommend $r \in [0.1, 0.2]$ together with a moderate N_s ratio.

We then studied the effect of point-cloud (PC) density. Performance varies nonlinearly with density. As shown in Table 8, reducing the PC density from 100% to 80% leaves the relative L_2 error essentially unchanged, indicating robustness to moderate downsampling. When the density drops to 40%, errors increase markedly due to the loss of fine geometric detail needed to capture local structure. Thus, modest downsampling can reduce compute with minimal accuracy loss, but aggressive sparsification should be avoided. Evaluating with denser PCs than those used in training only slightly affects accuracy when the training PC density is high (e.g., $\geq 60\%$), but yields accuracy improvement when the training PC density is low (e.g., 40%). These results confirm that reducing point-cloud density, which removes geometric detail, degrades accuracy.

4. Conclusions

In this work, we introduced the Geometry-Informed Neural Operator Transformer (GINOT), a novel framework for efficient and accurate solution prediction on arbitrary geometries represented by unordered, non-uniform, and

variable-sized surface point clouds, without the need for additional geometric features such as signed distance functions (SDFs). By utilizing transformer-based attention mechanisms and a geometry-aware encoding strategy, GINOT effectively captures geometric representations from boundary point clouds and maps them to solution fields at arbitrary query points. Unlike existing neural operator methods constrained by structured meshes, fixed query points, or computationally intensive geometric representations, GINOT offers a flexible and scalable approach for solving complex geometry problems. To enhance its functionality, we have integrated additional encoders to process problem-specific inputs, such as material properties and boundary conditions.

Extensive experiments on diverse datasets have demonstrated GINOT's good accuracy and generalization capabilities across various geometries. These results establish GINOT as a powerful surrogate model for computational physics involving complex domains, providing significant computational speedups while maintaining high predictive accuracy. Future work will focus on extending GINOT to tackle multi-physics problems, further enhancing its utility in scientific computing and engineering applications.

5. Data availability

The dataset is available on Zenodo [41] and the trained models are available at the GitHub repository <https://github.com/QibangLiu/GINOT>

6. Code availability

The codes for training and inference are available at the GitHub repository at <https://github.com/QibangLiu/GINOT>

7. Acknowledgements

The authors would like to thank the National Center for Supercomputing Applications (NCSA) at the University of Illinois, and particularly its Research Computing Directorate, Industry Program, and Center for Artificial Intelligence Innovation (CAII) for support and hardware resources. This research used both the DeltaAI advanced computing and data resource, which is supported by the National Science Foundation (award OAC 2320345) and the State of Illinois, and the Delta advanced computing and data resource which is supported by the National Science Foundation (award OAC 2005572) and the State of Illinois. Delta and DeltaAI are joint efforts of the University of Illinois Urbana-Champaign and its National Center for Supercomputing Applications. This work used Delta/DeltaAI at NCSA through allocations MAT240113 and CHE230009 from the Advanced Cyberinfrastructure Coordination Ecosystem: Services & Support (ACCESS) program, which is supported by U.S. National Science Foundation grants #2138259, #2138286, #2138307, #2137603, and #2138296.

8. Author contributions statement

Q. Liu conceptualized the study, developed the methodology, implemented the models, prepared the datasets, conducted the analysis, and drafted, reviewed, and edited the manuscript. **W. Zhong** contributed to running the baseline models, manuscript review and editing. **H. Meidani** contributed to conceptualization, results discussion, and manuscript review and editing. **D. Abueidda** contributed to results discussion and manuscript review and editing. **S. Koric** prepared the bracket lug dataset, contributed to conceptualization, results discussion, and reviewed and edited the manuscript. **P. Geubelle** contributed to the supervision, methodology, results discussion, and manuscript review and editing.

9. Competing interests statement

The authors declare no competing financial or non-financial interests.

References

[1] Q. Liu, D. Abueidda, S. Vyas, Y. Gao, S. Koric, P. H. Geubelle, Adaptive data-driven deep-learning surrogate model for frontal polymerization in dicyclopentadiene, *The Journal of Physical Chemistry B* 128 (2024) 1220–1230. doi:10.1021/acs.jpcb.3c07714.

[2] Y. Kihara, T. F. Heeren, C. S. Lee, Y. Wu, S. Xiao, S. Tzarisidis, F. G. Holz, P. C. Issa, C. A. Egan, A. Y. Lee, Estimating retinal sensitivity using optical coherence tomography with deep-learning algorithms in macular telangiectasia type 2, *JAMA network open* 2 (2019) e188029–e188029. doi:10.1001/jamanetworkopen.2018.8029.

[3] M. J. Ankenbrand, L. Shainberg, M. Hock, D. Lohr, L. M. Schreiber, Sensitivity analysis for interpretation of machine learning based segmentation models in cardiac mri, *BMC Medical Imaging* 21 (2021) 1–8. doi:10.1186/s12880-021-00551-1.

[4] E. M. Dogo, O. Afolabi, N. Nwulu, B. Twala, C. Aigbavboa, A comparative analysis of gradient descent-based optimization algorithms on convolutional neural networks, in: 2018 international conference on computational techniques, electronics and mechanical systems (CTEMS), IEEE, 2018, pp. 92–99. doi:10.1109/CTEMS.2018.8769211.

[5] M. S. Daoud, M. Shehab, H. M. Al-Mimi, L. Abualigah, R. A. Zitar, M. K. Y. Shambour, Gradient-based optimizer (gbo): a review, theory, variants, and applications, *Archives of Computational Methods in Engineering* 30 (2023) 2431–2449. doi:10.1007/s11831-022-09872-y.

[6] M. Abdar, F. Pourpanah, S. Hussain, D. Rezaazadegan, L. Liu, M. Ghavamzadeh, P. Fieguth, X. Cao, A. Khosravi, U. R. Acharya, et al., A review of uncertainty quantification in deep learning: Techniques, applications and challenges, *Information fusion* 76 (2021) 243–297. doi:10.1016/j.inffus.2021.05.008.

[7] J. Caldeira, B. Nord, Deeply uncertain: comparing methods of uncertainty quantification in deep learning algorithms, *Machine Learning: Science and Technology* 2 (2020) 015002. doi:10.1088/2632-2153/aba6f3.

[8] W. Zhong, H. Meidani, Pi-vae: Physics-informed variational auto-encoder for stochastic differential equations, *Computer Methods in Applied Mechanics and Engineering* 403 (2023) 115664. URL: <https://www.sciencedirect.com/science/article/pii/S0045782522006193>. doi:10.1016/j.cma.2022.115664.

[9] A. Chattopadhyay, M. Gray, T. Wu, A. B. Lowe, R. He, Oceanet: a principled neural operator-based digital twin for regional oceans, *Scientific Reports* 14 (2024) 21181.

[10] K. Kobayashi, S. B. Alam, Deep neural operator-driven real-time inference to enable digital twin solutions for nuclear energy systems, *Scientific reports* 14 (2024) 2101.

[11] K. Kobayashi, J. Daniell, S. B. Alam, Improved generalization with deep neural operators for engineering systems: Path towards digital twin, *Engineering Applications of Artificial Intelligence* 131 (2024) 107844.

[12] Q. Liu, P. Cai, D. Abueidda, S. Vyas, S. Koric, R. Gomez-Bombarelli, P. Geubelle, Univariate conditional variational autoencoder for morphogenetic pattern design in frontal polymerization-based manufacturing, *Computer Methods in Applied Mechanics and Engineering* 438 (2025) 117848. doi:10.1016/j.cma.2025.117848.

[13] Q. Liu, S. Koric, D. Abueidda, H. Meidani, P. Geubelle, Towards signed distance function based metamaterial design: Neural operator transformer for forward prediction and diffusion model for inverse design, *arXiv preprint arXiv:2504.01195* (2025). doi:10.48550/arXiv.2504.01195.

[14] Z. Li, N. Kovachki, K. Azizzadenesheli, B. Liu, K. Bhattacharya, A. Stuart, A. Anandkumar, Fourier neural operator for parametric partial differential equations, *arXiv preprint arXiv:2010.08895* (2020). doi:10.48550/arXiv.2010.08895.

[15] L. Lu, P. Jin, G. Pang, Z. Zhang, G. E. Karniadakis, Learning nonlinear operators via deepenet based on the universal approximation theorem of operators, *Nature machine intelligence* 3 (2021) 218–229. doi:10.1038/s42256-021-00302-5.

[16] N. Kovachki, S. Lanthaler, S. Mishra, On universal approximation and error bounds for fourier neural operators, *Journal of Machine Learning Research* 22 (2021) 1–76.

[17] H. You, Q. Zhang, C. J. Ross, C.-H. Lee, Y. Yu, Learning deep implicit fourier neural operators (ifnos) with applications to heterogeneous material modeling, *Computer Methods in Applied Mechanics and Engineering* 398 (2022) 115296.

[18] B. Bonev, T. Kurth, C. Hundt, J. Pathak, M. Baust, K. Kashinath, A. Anandkumar, Spherical fourier neural operators: Learning stable dynamics on the sphere, in: International conference on machine learning, PMLR, 2023, pp. 2806–2823.

[19] P. Cai, S. Liu, Q. Liu, P. H. Geubelle, R. Gomez-Bombarelli, Towards long rollout of neural operators with local attention and flow matching-inspired correction: An example in frontal polymerization PDEs, in: Machine Learning and the Physical Sciences Workshop @ NeurIPS 2024, 2024. URL: <https://openreview.net/forum?id=CFNgeuXzPx>.

[20] J. He, S. Koric, S. Kushwaha, J. Park, D. Abueidda, I. Jasiuk, Novel deepenet architecture to predict stresses in elastoplastic structures with variable complex geometries and loads, *Computer Methods in Applied Mechanics and Engineering* 415 (2023) 116277.

[21] W. Li, M. Z. Bazant, J. Zhu, Phase-field deepenet: Physics-informed deep operator neural network for fast simulations of pattern formation governed by gradient flows of free-energy functionals, *Computer Methods in Applied Mechanics and Engineering* 416 (2023) 116299.

[22] J. He, S. Kushwaha, J. Park, S. Koric, D. Abueidda, I. Jasiuk, Sequential deep operator networks (s-deepenet) for predicting full-field solutions under time-dependent loads, *Engineering Applications of Artificial Intelligence* 127 (2024) 107258.

[23] W. Zhong, H. Meidani, Physics-informed geometry-aware neural operator, *Computer Methods in Applied Mechanics and Engineering* 434 (2025) 117540.

[24] W. Zhong, H. Meidani, Physics-informed discretization-independent deep compositional operator network, *Computer Methods in Applied Mechanics and Engineering* 431 (2024) 117274.

[25] W. Zhong, Q. Liu, D. Abueidda, S. Koric, H. Meidani, A comprehensive comparison of neural operators for 3d industry-scale engineering designs, 2025. URL: <https://arxiv.org/abs/2510.05995>. arXiv:2510.05995.

[26] Z. Li, N. Kovachki, K. Azizzadenesheli, B. Liu, K. Bhattacharya, A. Stuart, A. Anandkumar, Neural operator: Graph kernel network for partial differential equations, *arXiv preprint arXiv:2003.03485* (2020). doi:10.48550/arXiv.2003.03485.

[27] Z. Li, D. Z. Huang, B. Liu, A. Anandkumar, Fourier neural operator with learned deformations for pdes on general geometries, *Journal of Machine Learning Research* 24 (2023) 1–26. URL: <http://jmlr.org/papers/v24/23-0064.html>.

[28] Z. Li, N. Kovachki, C. Choy, B. Li, J. Kossaifi, S. Otta, M. A. Nabian, M. Stadler, C. Hundt, K. Azizzadenesheli, A. Anandkumar, Geometry-informed neural operator for large-scale 3d pdes, in: A. Oh, T. Naumann, A. Globerson, K. Saenko, M. Hardt, S. Levine (Eds.), *Advances in Neural Information Processing Systems*, volume 36, Curran Associates, Inc., 2023, pp. 35836–35854.

- [29] J. He, S. Koric, D. Abueidda, A. Najafi, I. Jasiuk, Geom-deeponet: A point-cloud-based deep operator network for field predictions on 3d parameterized geometries, *Computer Methods in Applied Mechanics and Engineering* 429 (2024) 117130. doi:10.1016/j.cma.2024.117130.
- [30] A. Vaswani, N. Shazeer, N. Parmar, J. Uszkoreit, L. Jones, A. N. Gomez, L. u. Kaiser, I. Polosukhin, Attention is all you need, in: I. Guyon, U. V. Luxburg, S. Bengio, H. Wallach, R. Fergus, S. Vishwanathan, R. Garnett (Eds.), *Advances in Neural Information Processing Systems*, volume 30, Curran Associates, Inc., 2017.
- [31] S. Cao, Choose a transformer: Fourier or galerkin, *Advances in neural information processing systems* 34 (2021) 24924–24940.
- [32] X. Liu, B. Xu, L. Zhang, Ht-net: Hierarchical transformer based operator learning model for multiscale pdes (2022).
- [33] Z. Li, K. Meidani, A. B. Farimani, Transformer for partial differential equations' operator learning, *arXiv preprint arXiv:2205.13671* (2022). doi:10.48550/arXiv.2205.13671.
- [34] Z. Hao, Z. Wang, H. Su, C. Ying, Y. Dong, S. Liu, Z. Cheng, J. Song, J. Zhu, Gnot: A general neural operator transformer for operator learning, in: *International Conference on Machine Learning*, PMLR, 2023, pp. 12556–12569.
- [35] H. Jun, A. Nichol, Shap-e: Generating conditional 3d implicit functions, *arXiv preprint arXiv:2305.02463* (2023). doi:10.48550/arXiv.2305.02463.
- [36] C. R. Qi, H. Su, K. Mo, L. J. Guibas, Pointnet: Deep learning on point sets for 3d classification and segmentation, in: *Proceedings of the IEEE conference on computer vision and pattern recognition*, 2017, pp. 652–660.
- [37] C. R. Qi, L. Yi, H. Su, L. J. Guibas, Pointnet++: Deep hierarchical feature learning on point sets in a metric space, *Advances in neural information processing systems* 30 (2017).
- [38] B. Mildenhall, P. P. Srinivasan, M. Tancik, J. T. Barron, R. Ramamoorthi, R. Ng, Nerf: Representing scenes as neural radiance fields for view synthesis, *Communications of the ACM* 65 (2021) 99–106. doi:10.48550/arXiv.2003.08934.
- [39] Q. Liu, Dataset for "towards signed distance function based metamaterial design: Neural operator transformer for forward prediction and diffusion model for inverse design", 2025. doi:10.5281/zenodo.15121966.
- [40] S. Hong, Y. Kwon, D. Shin, J. Park, N. Kang, Deepjeb: 3d deep learning-based synthetic jet engine bracket dataset, *Journal of Mechanical Design* 147 (2024). doi:10.1115/1.4067089.
- [41] Q. Liu, Dataset for "geometry informed neural operator transformer", 2025. URL: <https://doi.org/10.5281/zenodo.15293036>, data set. doi:10.5281/zenodo.15293036, data set.

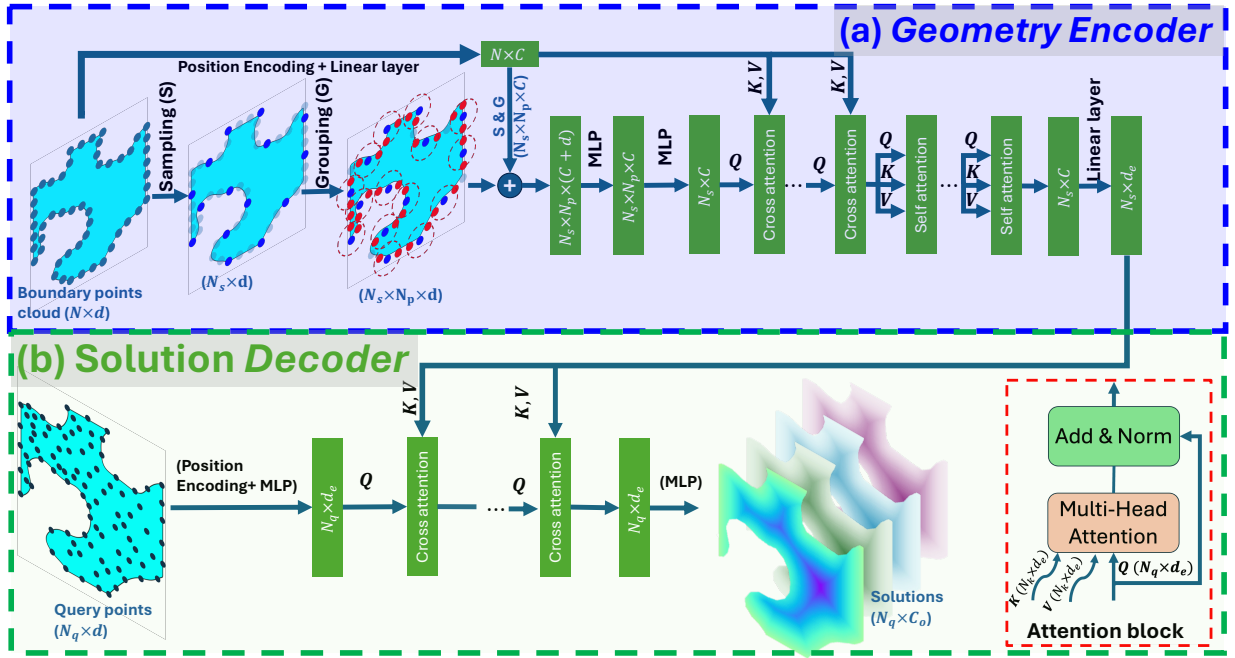


Fig. 1: Overview of the Geometry-Informed Neural Operator Transformer (GINOT) architecture. The boundary point cloud is initially processed through sampling and grouping layers to extract local geometric features. These local features are then fused with global geometric information via a cross-attention layer. This is followed by a series of self-attention layers and a final linear layer, producing the KEY and VALUE matrices for the cross-attention layer in the solution decoder. In the solution decoder, an multilayer perceptron (MLP) encodes the query points into the QUERY matrix for the cross-attention layer, which integrates the geometry information from the encoder. The output of the cross-attention layer is subsequently decoded into solution fields at the query points using another MLP.

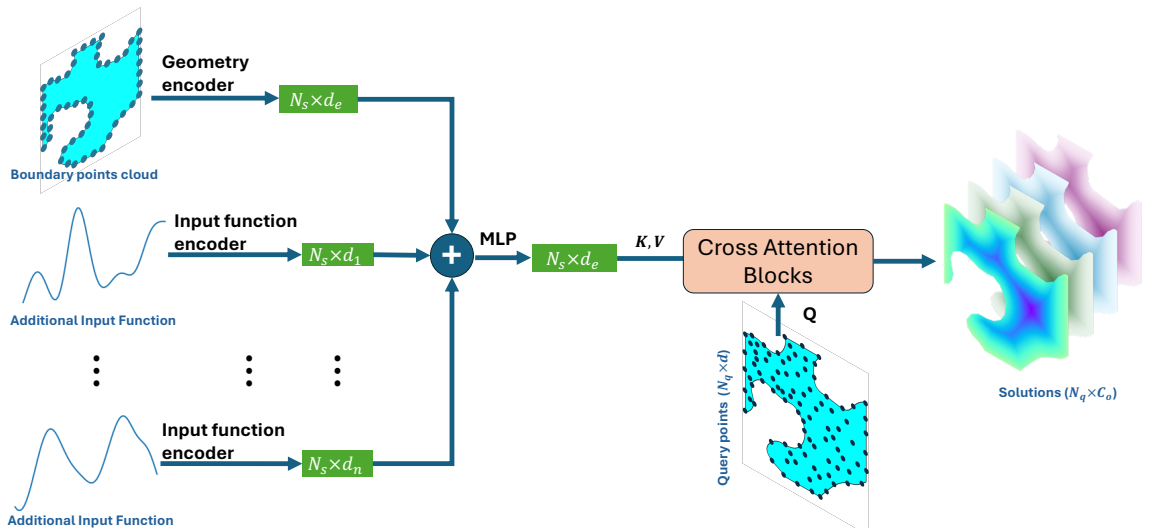


Fig. 2: Extending GINOT for additional inputs. Encoders for extra inputs process these features, which are then concatenated with the geometry encoder's output. The combined representation is passed through an MLP for aggregation and used as the KEY and VALUE in the solution decoder's cross-attention blocks. This extension enables GINOT to incorporate both geometric and non-geometric inputs effectively.

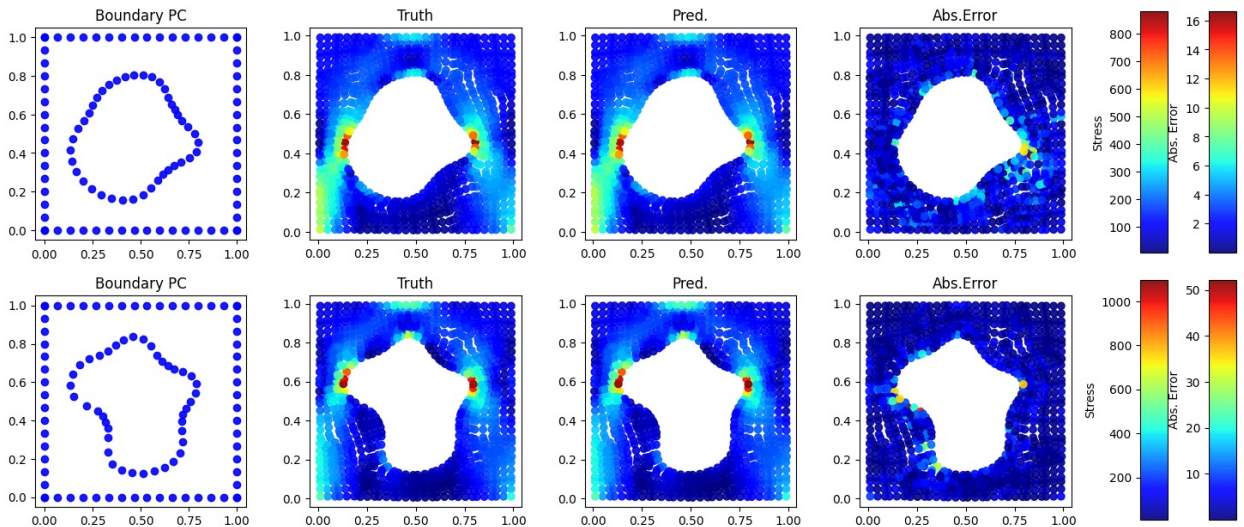


Fig. 3: Stress solutions of the testing sample for the elasticity problem. The first row shows the median case ($L_2 = 1.23\%$), while the second row represents the worst case ($L_2 = 2.93\%$) based on L_2 relative error. The first column depicts the input surface point cloud, the second column presents the ground truth from finite element analysis, the third column shows the prediction by GINOT, and the last column highlights the absolute error between the prediction and the ground truth.

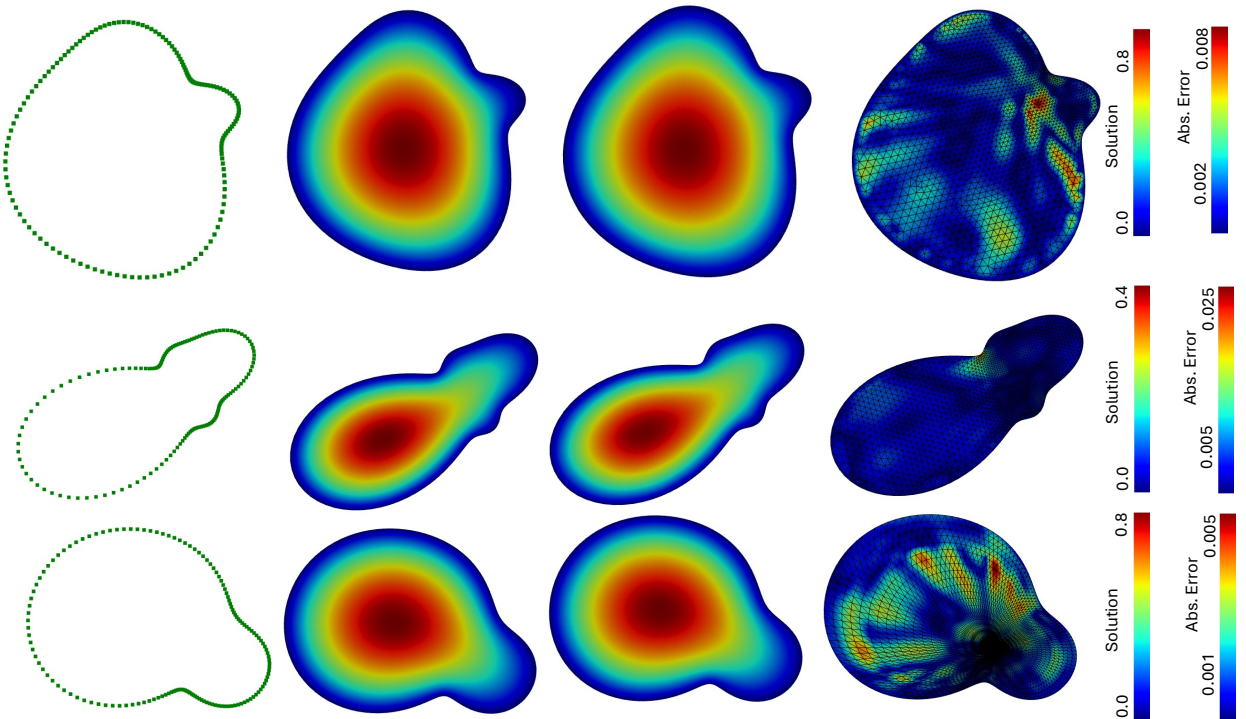


Fig. 4: Testing sample solutions for the Poisson equation. The first row shows the median case ($L_2 = 0.41\%$) while the second row presents the worst case ($L_2 = 2.27\%$) for unstructured mesh data, based on L_2 relative error. The third row displays the median case ($L_2 = 0.38\%$) for structured mesh data. The first column illustrates the input surface point cloud, the second column shows the FEM ground truth, the third column provides GINOT predictions, and the last column highlights the absolute error between predictions and the ground truth. Structured and unstructured meshes are also depicted in the last column.

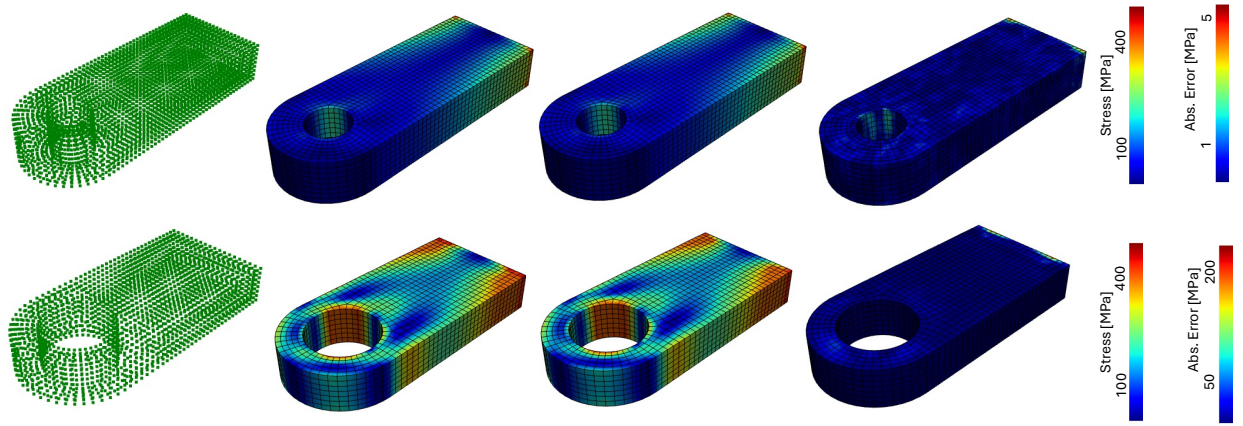


Fig. 5: Stress solutions for the testing samples of bracket lugs. The first row shows the median case ($L_2 = 0.41\%$), while the second row represents the worst case ($L_2 = 3.78\%$) based on L_2 relative error. The first column illustrates the input surface point cloud, the second column presents the ground truth from finite element analysis, the third column shows the GINOT prediction, and the last column highlights the absolute error between the prediction and the ground truth.

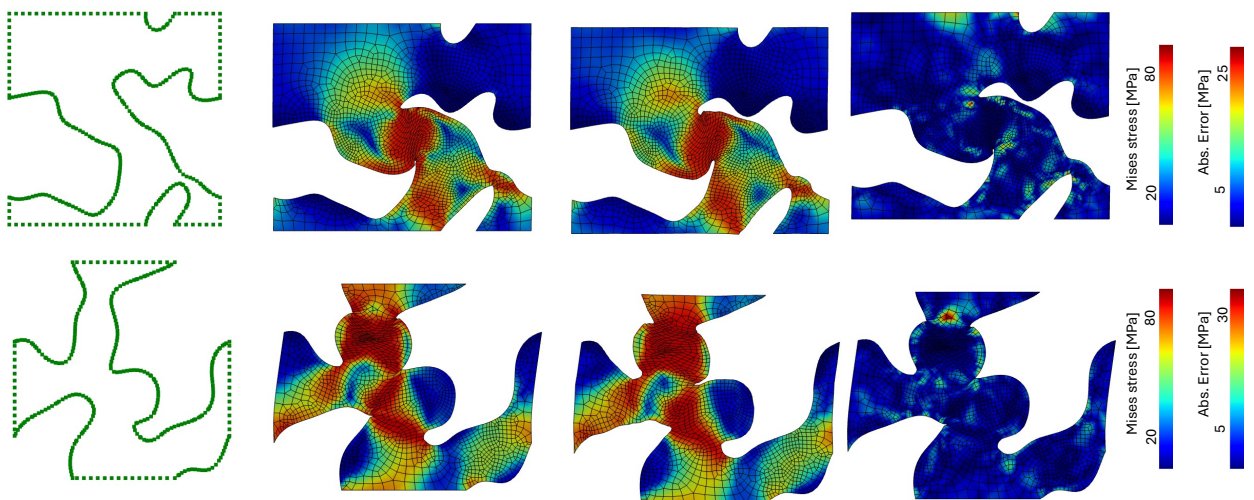


Fig. 6: Mises stress and displacement solutions at the final strain step for the testing sample of the micro-periodic unit cell. The first row shows the median case ($L_2 = 7.54\%$), while the second row represents the 95th percentile case ($L_2 = 13.03\%$) based on L_2 relative error. The first column illustrates the input surface point cloud, the second column displays the true stress on the true deformed shape, the third column shows the predicted stress on the predicted deformed shape, and the last column highlights the absolute error of stress on the true deformed shape.

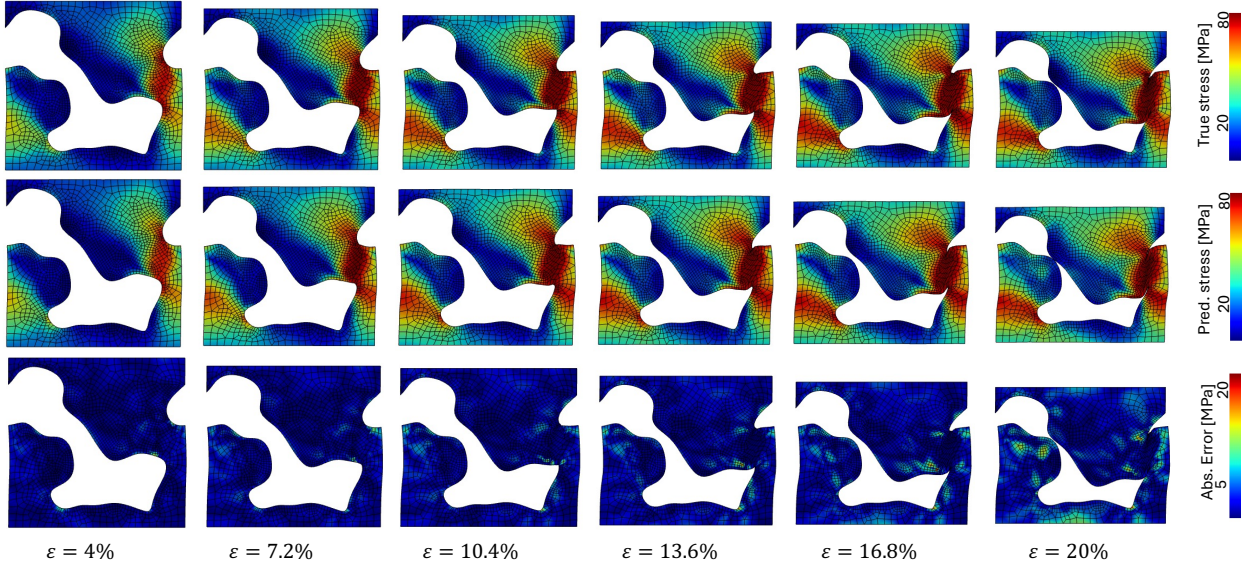


Fig. 7: Mises stress and displacement solutions across historical strain steps for the median testing sample ($L_2 = 9.08\%$) of the micro-periodic unit cell, based on L_2 relative error. The first row shows the true stress on the true deformed shape, the second row presents the predicted stress on the predicted deformed shape, and the last row highlights the absolute error of the stress on the true deformed shape.

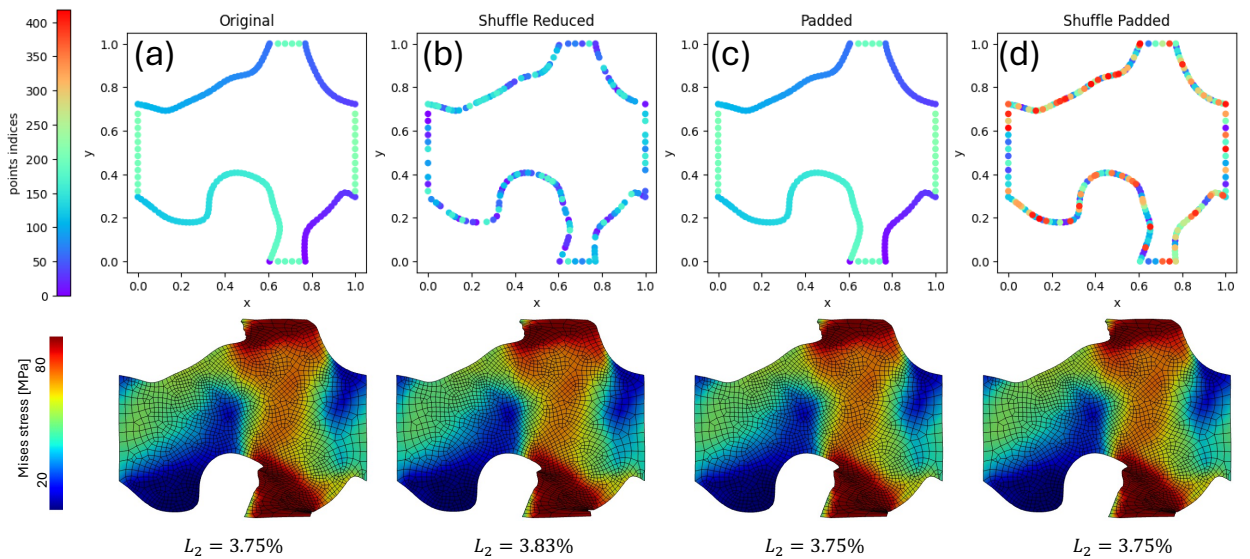


Fig. 8: Demonstrating the versatility of the geometry encoder. The first row illustrates the input surface point cloud, with colors indicating the point order. The second row presents the corresponding predicted Mises stress on the predicted deformed shape by GINOT. (a) Original surface point cloud (PC) with 220 points, (b) shuffled original PC with the first 80% retained, (c) original PC padded with 199 points at coordinates (-1000, -1000) (not shown), and (d) shuffled version of the PC in (c). The L_2 relative errors for each case are displayed at the bottom.

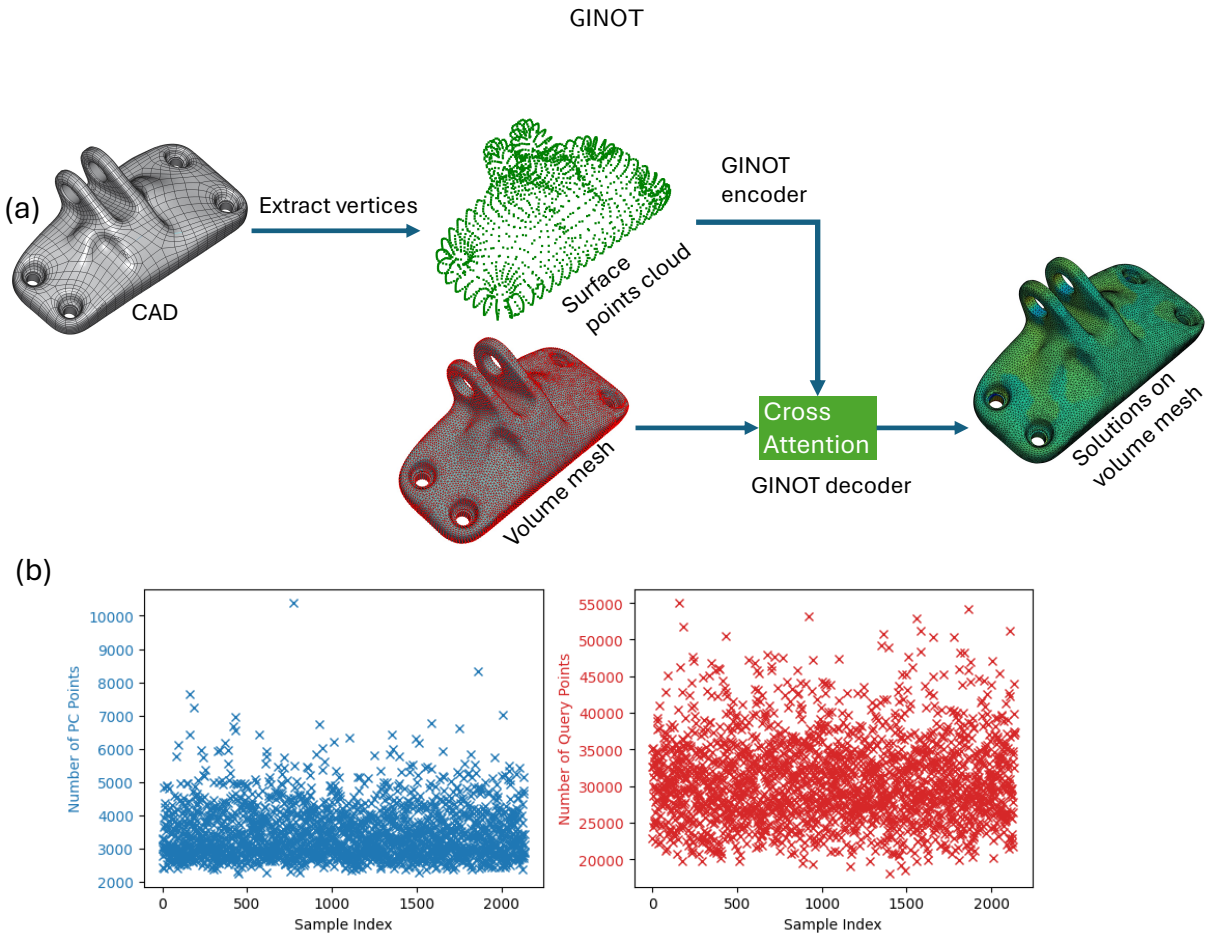


Fig. 9: Workflow for the Jet Engine Bracket (JEB) dataset. (a) Boundary points clouds are extracted from the CAD models of each JEB sample using FreeCAD with PythonAPI and serve as input to the geometry encoder of GINOT. The 3D volume mesh nodes are utilized as query points and provided to the solution decoder of GINOT. (b) Distribution of the number of boundary points in the cloud and volume mesh nodes across the 2138 JEB samples.

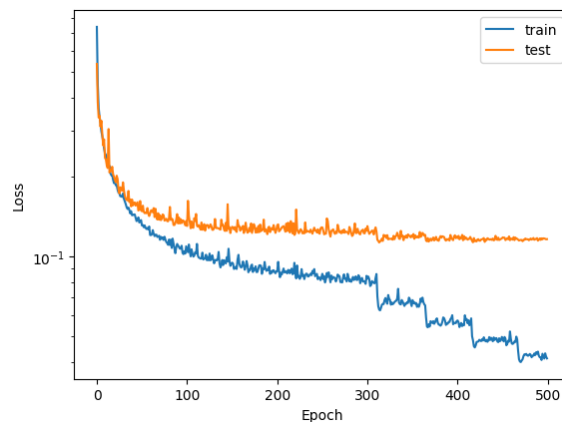


Fig. 10: Training and validation mean squared error (MSE) loss curves for GINOT on the JEB dataset.

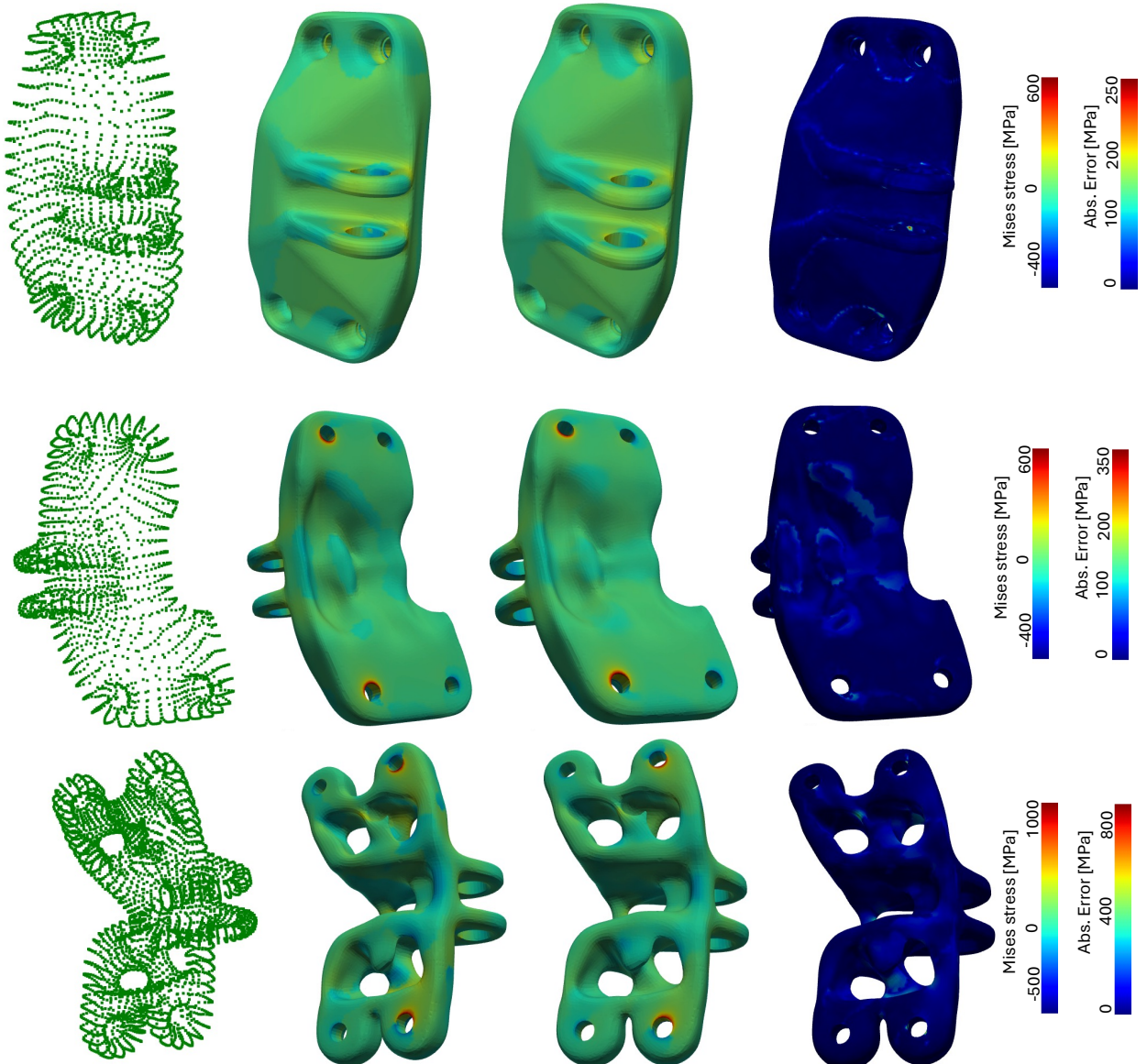


Fig. 11: Mises stress solutions for the testing samples of the JEB dataset. The first row shows the best case ($L_2 = 16.99\%$), the second row represents the median case ($L_2 = 29.0\%$), and the third row depicts the worst case ($L_2 = 54.86\%$). The first column illustrates the input surface point cloud, the second column presents the ground truth from finite element analysis, the third column shows the GINOT prediction, and the last column highlights the absolute error between the prediction and the ground truth.